

UC Irvine

UC Irvine Previously Published Works

Title

Dynamic Model for Understanding Spatial Temperature and Species Distributions in Internal-Reforming Solid Oxide Fuel Cells

Permalink

<https://escholarship.org/uc/item/0z771690>

ISBN

978-0-7918-4881-4

Authors

Shaffer, Brendan
Brouwer, Jacob

Publication Date

2009

DOI

10.1115/fuelcell2009-85095

Copyright Information

This work is made available under the terms of a Creative Commons Attribution License, available at <https://creativecommons.org/licenses/by/4.0/>

Peer reviewed

FuelCell2009-85095

DYNAMIC MODEL FOR UNDERSTANDING SPATIAL TEMPERATURE AND SPECIES DISTRIBUTIONS IN INTERNAL-REFORMING SOLID OXIDE FUEL CELLS

Brendan Shaffer and Jacob Brouwer*

National Fuel Cell Research Center

University of California, Irvine, California, 92697-3550

*corresponding author: jb@nfcrc.uci.edu; tel: 949-824-1999; fax: 949-824-7423

ABSTRACT

Direct internal reformation of methane in solid oxide fuel cells (SOFCs) leads to two major performance and longevity challenges: thermal stresses in the cell due to large temperature gradients and coke formation on the anode. A simplified quasi-two-dimensional direct internal reformation SOFC (DIR-SOFC) dynamic model was developed for investigation of the effects of various parameters and assumptions on the temperature gradients across the cell. The model consists of 64 nodes each of which contains four control volumes: the positive electrode, electrolyte, negative electrode (PEN); interconnect; anode gas; and cathode gas. Within each node the corresponding conservation, chemical, and electrochemical reaction equations are solved. The model simulates the counterflow configuration since previous research [8] has shown this configuration to yield the smallest temperature differentials. Steady state simulations revealed several results where the temperature difference across the cell was considerably affected by operating and cell design parameters. Increasing the performance of the cell through modifications to the electrochemical model to simulate modern cell performance produced significant changes in the cell temperature differential. Improved cell performance led to a maximum increase in the temperature differential across the cell of 31 K. An increase in the interconnect thickness also exhibits a considerable reduction in the temperature difference across the PEN. In particular, increasing the interconnect thickness from 3.5 to 4.5 mm can achieve about a 50 K reduction in the cross cell temperature difference. Variation of other physical parameters such as the thermal conductivity of the interconnect and the rib width also showed an effect on the temperature distribution. The sensitivity of temperature distribution to the adiabatic assumption was also performed and results showed a considerable effect near the fuel and air

inlets. This resulted in severe temperature gradients approaching 160 K/cm.

INTRODUCTION

Solid oxide fuel cells show promise as a future stationary power generation device. Given the recent SECA improvements [1] this technology's proximity to commercial emergence grows closer at an ever increasing rate. The SOFC's ability for direct internal reformation of hydrocarbon fuels, and in particular natural gas, provides the incentive of using the existing fuel infrastructure. This characteristic also allows the co-production of hydrogen, which may help mobilize the expansion of a hydrogen infrastructure. These qualities make the SOFC especially suited for large scale deployment as a power generation source in an incipient hydrogen economy.

Despite this optimistic outlook, the present situation recognizes several impediments to the reliability of DIR-SOFC technology. The first is coking of the hydrocarbon fuel on the anode. Coking results in the deactivation of reaction sites and the clogging of pores. Some publications have shown coking to be a minor problem when operating at high temperatures and steam to carbon ratios [2,3]. However, the focus of much SOFC research has been on the reduction of operating temperature to reduce degradation, improve efficiency, and allow for better seals to be used. The use of high steam to carbon ratios also dilutes the fuel in the anode channel thereby reducing performance. Despite these drawbacks to operating at high temperatures and steam to carbon ratios, this paper will consider these conditions so as to avoid the issue of coking and focus on the second impediment, which is the presence of high thermal stresses due to the excessive thermal gradients across the PEN resulting from the imbalance of the endothermic reformation and exothermic electrochemical reactions.

A dynamic quasi-two dimensional planar SOFC model is developed for the investigation of thermal gradients within DIR-SOFCs. The finite volume model consists of 64 nodes each of which contains 5 control volumes. A complete discussion of the model is in the following section.

MODEL

The dynamic DIR-SOFC model is modeled using the MATLAB Simulink® platform. The finite volume approach has been dubbed by some as being more appropriate for the modeling of SOFCs because it may approximate the physical processes better [4].

The cell was divided into 64 nodes as seen in Figure 1. Each node consists of five control volumes: the interconnects, anode and cathode compartments, and the PEN.

Most of the assumptions used in this model are the same as those used by Mueller et al. [5], which include but are not limited to the following:

- (1) The fuel cell is well insulated such that heat loss from the cell is negligible.
- (2) The flow in the fuel cell is laminar.
- (3) Pressure drops are negligible.
- (4) The gases are ideal and incompressible.
- (5) Radiation heat transfer is negligible. [6,7]
- (6) Conduction along the PEN is negligible since conduction through the interconnect dominates.
- (7) Coking is negligible due to the high steam to carbon ratio used in the following analyses. [2,3]
- (8) The water gas shift reaction is assumed to be in equilibrium.
- (9) Both electrodes exhibit high enough conductivity that it is assumed that both are an equi-potential surface.
- (10) Only hydrogen participates in the electrochemical reaction at the anode.
- (11) The electrochemistry is rapid such that the rate of reaction is proportional to the current.

The cell is in the counter-flow configuration as shown in Figure 1. This flow configuration has been shown to have the lowest temperature difference across the cell [8]. For the purposes of plotting the fuel flow designates the direction of the abscissa axis.

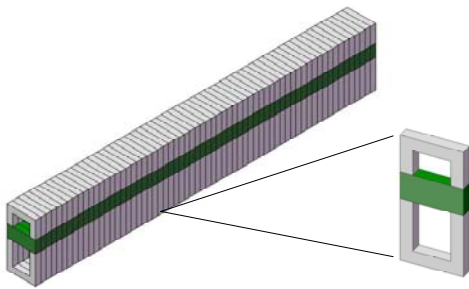


Figure 1. Schematic of the solid oxide fuel cell model.

Electrochemical Model

The equipotential assumption allows the input of a cell voltage for which the electrochemical model solves for a current such that the specified voltage is met. The electrochemical model is defined by the equation for the cell voltage shown below:

$$V = E_{OCV} - \eta_{act} - \eta_{ohm} - \eta_{conc} \quad (1)$$

The first term in the preceding equation is the Nernst voltage calculated using the following equation:

$$E_{Nernst} = E_0 - \frac{R_u T_{PEN}}{nF} \ln \left(\frac{P_{H_2O}}{P_{H_2} P_{O_2}^{1/2}} \right) \quad (2)$$

The first term in the Nernst equation is the reversible potential and is calculated from the Gibb's free energy using the equation and polynomial below.

$$E_0 = -\frac{\Delta G}{nF}$$

$$\Delta G = (-2.4087E - 9 \cdot T_{PEN}^3 + 1.0641E - 5 \cdot T_{PEN}^2 \dots \dots + 0.0411 \cdot T_{PEN} - 241.9459) \cdot 1000 \quad (3)$$

The second term represents what has been termed the Nernstian losses. These losses are a result of the bulk reactant concentrations seen in the anode and cathode channels. The Nernst voltage corresponds to the voltage of the cell at open circuit pending there is no current leakage across the electrolyte, anode/cathode gas leakage, etc. The other terms in the equation for the cell voltage attempt to describe the remaining losses: activation, concentration, and ohmic polarizations. The activation polarization results from the existence of an activation barrier at each electrode which the reactants need to overcome for reaction to occur at a certain rate. This barrier is surmounted by the use of some of the useful voltage such that the activation barrier is lowered sufficiently. Using the Butler-Volmer model of activation polarization and assuming activation losses occur only at the cathode with a transfer coefficient of 0.5, the following equation is derived for the activation polarization:

$$\eta_{act} = \frac{2R_u T_{PEN}}{nF} \sinh^{-1} \left(\frac{I}{2j_0 A} \right) \quad (4)$$

The assumption of cathode activation losses only is fairly accurate since cathode activation losses dominate, however the above equation is a semi-empirical equation for which the exchange current density parameter, j_0 , is usually empirically determined from experiment such that a fit to a experimental V-I curve is obtained by the model. Therefore, although the activation polarization equation has its roots in first principles the practical use of the equation requires some empirical curve fitting, which may include other parameters in addition to the exchange current such that a fit is obtained. This concept of curve fitting follows for the rest of the loss models.

The concentration polarization results from a lack of sufficient supply of reactants to the triple phase boundary such that the reaction occurs at a reduced rate for a given voltage. This loss ultimately results in the failure of the cell's ability to produce power. As the user continues to increase the load on the cell, the reactants at the triple phase boundaries decrease until there are no more reactants at the TPBs such that the cell produces no current. The current at which this occurs is termed the limiting current density. The equation describing this voltage loss mechanism is:

$$\eta_{conc} = -\frac{R_u T_{PEN}}{nF} \ln \left(1 - \frac{I}{j_L A} \right) \quad (5)$$

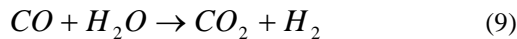
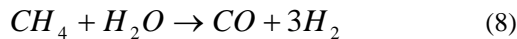
Ohmic polarizations are those losses due to electronic and ionic resistances within the cell and the cell assembly which could include the interconnect, contact resistances between the electrolyte/electrode interfaces, contact resistances between the electrode/interconnect interfaces, etc. The ohmic resistance of the cell used in this paper was adapted from the experimental data given by Kim [9]. The following equation is used within the cell model:

$$\eta_{ohm} = i R_{PEN} (T_{PEN}) \quad (6)$$

$$R_{PEN} = T_{PEN} \cdot e^{C1/T_{PEN} + C0} \quad (7)$$

Reformation Reactions

The direct operation of the SOFC on natural gas requires the model to account for the reformation reactions and the kinetics associated with them. The natural gas is assumed to be pure methane in this paper. The following reactions are the steam methane reformation (SMR) reaction and the water gas shift (WGS) reaction.



The SMR is endothermic and the WGS reaction is exothermic, however, their combined reaction is still endothermic. The possibility of balancing this endothermicity with the exothermicity of the electrochemical reaction was one of the original motivations for investigating direct internal reformation [8].

A number of attempts to assess empirical expressions accurately depicting SMR kinetics have been performed. Some of these experimental studies did not use materials germane to solid oxide fuel cell anodes [10]. Earlier DIR-SOFC publications such as [11] used kinetic data from [12] citing that their data was typical of SMR on SOFC anodes.

$$R = \pm \nu k_0 P_{CH_4} A \left(1 - \frac{Q}{K_{eq}} \right) e^{-E_a/R_u T} \quad (10)$$

In the above equation, R is the rate of reaction of equation; the coefficient ν is the stoichiometric coefficient of the particular species; the pre-exponential factor k_0 is $4.274 \text{ kmol}/(\text{m}^2\text{-s-}$

bar); the partial pressure of methane is P_{CH_4} in bars; A is the surface area of the node; Q is the reaction quotient; K_{eq} is the equilibrium constant; the activation energy E_a is $82,000 \text{ kJ/kmol}$; the universal gas constant R_u is $8.314 \text{ kJ}/(\text{kmol-K})$; and T is the temperature of the node.

The water gas shift reaction is assumed to be at equilibrium as mentioned previously. Ahmed and Foger [13] examined this assumption experimentally in their 2001 publication and found it to be true for typical SOFC conditions and at high levels of fuel utilization. For low levels of fuel utilization it was found that the WGS reaction did not approach equilibrium. The rate of reaction for the WGS reaction is shown below

$$R = \pm \nu k_0 P_{CO} A \left(1 - \frac{Q}{K_{eq}} \right) \quad (11)$$

This equation was adapted from Aguiar [11]. The pre-exponential constant, k_0 , is a number large enough such that the rate of reaction equation is representative of equilibrium.

Conserved Quantities: Mass and Energy

The conserved quantities are only mass and energy disregarding momentum due to the assumption of constant pressure. This assumption has been shown by other publications to achieve results similar to those models without this assumption [14]. The use of this assumption allows a substantial reduction in computational intensity. The conservation equations of mass and energy have different characteristic times associated with them depending on the particular control volume they are describing. For example, the cathode compartment experiences much higher flow rates than the anode compartment resulting in different residence/characteristic times. To avoid these issues associated with differing characteristic times, a variable time step solver was used. The variable time-step solver selects a period that is below the smallest characteristic time so that it might well and simultaneously solve all of the integral conservation equations.

Mass

Within each gas control volume the total number of moles is conserved using the equation:

$$\frac{dN}{dt} = \dot{N}_{in} + \sum R - \dot{N}_{out} \quad (12)$$

This equation written for an individual species is:

$$\frac{d}{dt}(NX_{out}) = \dot{N}_{in} X_{in} + R - \dot{N}_{out} X_{out} \quad (13)$$

Invoking the perfectly stirred reactor assumption, where diffusional fluxes are ignored, the properties at the exit of each CV may be assumed to be equivalent to the properties of the entire CV. With this PSR assumption and the assumption that

$$\frac{d(NX_{out})}{dt} \cong N \frac{d(X_{out})}{dt}, \quad (14)$$

the equation can be manipulated such that an integration in time can be performed for the concentration of the species at the exit and hence within the entire CV.

$$X_{out} = \frac{R_u T_{out}}{PV} \int (\dot{N}_{in} X_{in} + R - \dot{N}_{out} X_{out}) dt \quad (15)$$

where

$$N = \frac{PV}{R_u T_{out}} \quad (16)$$

because all gases considered in this model are ideal; the Ideal gas Law can be summoned.

Energy

The conservation of energy is applied to the five CVs, which consist of two different phases of matter: solid and gas. The interaction between the phases is through convective heat transfer only using Newton's Law of Cooling to model this process.

$$\dot{Q}_{conv} = hA_i(T_i - T_{out}) \quad (17)$$

The convection coefficient, h , is determined using the equation for the Nusselt number. The Nusselt number for the typical dimensions of the gas channels in the fuel cell is 3.8 [15].

$$h = \frac{k}{D_h} Nu \quad (18)$$

The hydraulic diameter is defined as four times the cross sectional area of the flow divided by the wetted perimeter. The thermal conductivity of the gas is calculated using the following approximation:

$$k = \sum X_i k_i(T_{out}) \quad (19)$$

Radiation is assumed negligible. The solid CVs interact energetically through conductive heat transfer modeled using Fourier's Law.

$$\dot{Q}_{cond} = kA \frac{\Delta T}{L} \quad (20)$$

PEN

Application of conservation of energy to the PEN yields the following:

$$\frac{dU_{PEN}}{dt} = \dot{E}_{gen} + \sum \dot{Q}. \quad (21)$$

The change in the internal energy of the PEN control volume is equivalent to the sum of the heat transferred to the CV and the heat generated within the CV. The heat generated within the PEN results from the exothermic electrochemical reaction occurring at its TPBs. The heat generated can be described by the following:

$$\dot{E}_{gen} = R_{O_2} h_{O_2}(T_{out}) + R_{H_2O} h_{H_2O}(T_{PEN}) + R_{H_2} h_{H_2}(T_{out}) - IV. \quad (22)$$

Since the PEN is a solid (although porous in the electrodes), the specific heat is constant leading to the equation:

$$T_{PEN} = \frac{1}{\rho_{PEN} c_{PEN} V} \int (\dot{E}_{gen} + \sum \dot{Q}) dt. \quad (23)$$

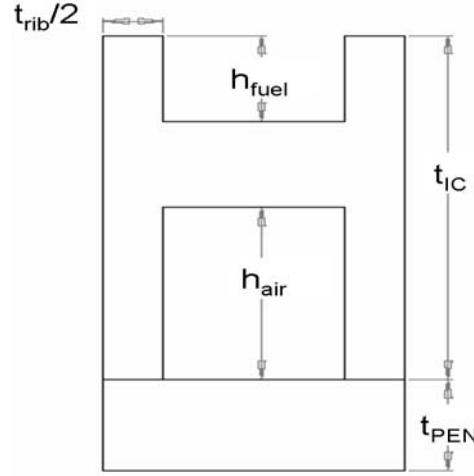


Figure 2. Fuel Cell Dimensions.

Interconnect

The interconnect temperature is solved for in the same manner except for the lack of heat generation within the interconnect. The conservation of energy renders the following:

$$\frac{dU_{int}}{dt} = \sum \dot{Q}. \quad (24)$$

The internal energy of the interconnect control volume depends simply upon the heat transferred to/from it. As in the case of the PEN, the temperature of the interconnect can be calculated by integrating the sum of the heat transfers in time and dividing that by the product of the density, specific heat, and volume.

Anode and Cathode Gases

The general equations of these two control volumes are identical. Conservation of energy results in the following:

$$\frac{dU}{dt} = \dot{H}_{in} + \dot{H} - \dot{H}_{out} + \sum \dot{Q}. \quad (25)$$

Since the anode and cathode gases are assumed to be ideal gases the internal energy is a function of only temperature hence

$$dU = Nc_v dT. \quad (26)$$

Assuming that the anode and cathode gases are ideal gases allows the calculation of the temperature of the control volume.

$$T = \frac{R_u T}{PVC_v(T)} \int (\dot{H}_{in} - \dot{H}_{out} + \sum \dot{Q}) dt \quad (27)$$

TABLE 1. MODEL PARAMETERS

Parameter	Value	Units
PEN thickness	1.06	mm
PEN Density	5900	kg/m ³
PEN Specific Heat	0.5	kJ/kg-K
PEN Thermal Conductivity	2	W/m-K
IC thickness	4	mm
IC Density	9000	kg/m ³
IC Specific Heat	0.62	kJ/kg-K
IC Thermal Conductivity	25	W/m-K
C1	7509.6	
Cathode Channel Ht.	2	mm
Anode Channel Ht.	1	mm
Cell Width	0.25	cm
Cell Length	10	cm
Cell Active Area	2.5	cm ²

ELECTROCHEMICAL PARAMETER DETERMINATION

The SECA performance improvements have been considerable as seen in the following figure.

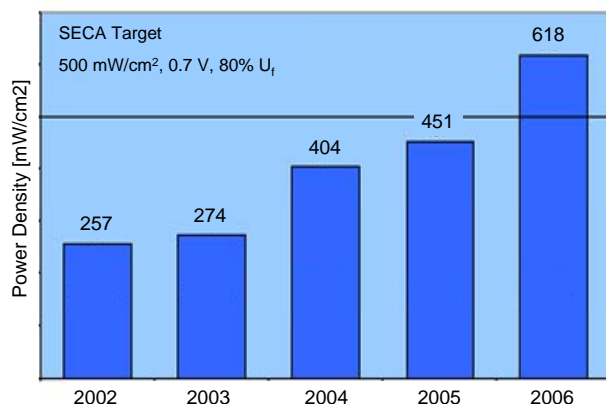


Figure 3. SECA improvements (adapted from [1]).

These performance improvements may have an impact on the thermal and concentration gradients within the cell. These impacts will be investigated by adjusting the electrochemical model parameters such that the experimental data from these better performing cells is matched by the model. These electrochemical model parameters include the exchange current density, the C0 constant in the temperature dependent resistance equation, and the limiting current density. The experimental data used are from a presentation at the 9th SECA Workshop and are representative of Versa Power SOFCs [16]. It is expected and some data has shown that the improvements are better than those seen by the Versa Power data. However, the information accompanying these data is limited, therefore it was decided to use the Versa Power data,

which includes flow rates. The operating conditions for these data are shown below in Table 2.

TABLE 2. OPERATING CONDITIONS FOR VERSA POWER CELL

Operating Temperature	973 K
Active Area	81 cm ²
Fuel Flowrate	2 SLPM
Air Flowrate	2 SLPM
V _{cell}	0.85 V
j _{cell}	740 mA/cm ²

The concentration loss was approximated so as to reasonably represent the losses corresponding to the utilizations of fuel and air. The same limiting current density was used in the high and low performance cell simulations. The high performance experimental data was matched by adjusting only the exchange current density and the C0 constant in the temperature dependent resistance equation. The table below summarizes the parameters used for the high and low performance cells.

TABLE 3. PERFORMANCE PARAMETERS FOR TABLE 2 OPERATING CONDITIONS

	High	Low	Units
j _o	2700	1000	A/m ²
C0	-25.94	-25.855	[-]
j _L	35000	35000	A/m ²

The low performance cell was characterized using typical electrochemical model parameters found within literature [9,17,18].

These parameters have been used assuming an operation on humidified hydrogen at a temperature of 700 C with low fuel and air utilizations. However, the focus of this paper is the investigation of direct internal reforming at realistic operating conditions. Therefore, a higher operating temperature range of 1123-1173 K is more appropriate in order to avoid extensive coking [2,3]. As the temperature increases so too will the exchange current density. The exchange current densities used for the high and low performance cells at these increased temperatures are 5000 A/m² and 2000 A/m², respectively. The low performance cell exchange current density was chosen from the existing literature. The high performance cell value was then chosen assuming that the exchange current would follow the same trend approximately. Therefore, the high performance exchange current at the lower temperature would need to be approximately doubled, however the value in Table 4 shows that the value was not doubled in an effort to be conservative with respect to the performance. Higher fuel and air utilizations are also needed to minimize losses. As the utilizations are increased the limiting current density will

decrease. The limiting current density was approximated based on the corresponding utilizations. Throughout the rest of the paper these values will be used in the simulations unless otherwise stated.

TABLE 4. PERFORMANCE PARAMETERS FOR OPER. TEMP. OF 1123-1173 K

	High	Low	Units
j_0	5000	2000	A/m ²
C0	-25.94	-25.855	[-]
j_L	17000	17000	A/m ²

ANALYSIS, RESULTS, AND DISCUSSION

Performance and Fuel Composition Variation

The following fuel compositions were analyzed for both the high and low performance cells. The partial reformation composition was determined by assuming that the pure mixture was in equilibrium at 800 K. The syngas composition was determined from NETL data. The inlet temperatures for the air and fuel flows were varied such that the average PEN temperature was maintained within 1123-1173 K.

TABLE 5. FUEL COMPOSITIONS

	No Pre-Reforming	Partial Pre-Reforming	Syngas
CH ₄	0.25	0.091	0.17
CO	0	0.017	0.05
CO ₂	0	0.089	0.215
H ₂	0	0.405	0.125
H ₂ O	0.75	0.398	0.391
N ₂	0	0	0.049
T _{inlet}	973	923	948

The operation parameters for these fuel composition variations are shown in Table 6.

TABLE 6. OPERATION PARAMETERS FOR FUEL COMPOSITION VARIATION

Avg. PEN Temperature	1123-1173 K
Fuel Utilization	0.85
Air Utilization	0.25
V _{cell}	0.7 V

No Pre-Reformation

The no pre-reformation simulations confirmed that the electrochemical performance does have an effect on the PEN temperature. In Figure 5, the peak temperature has increased while the average PEN temperature has only increased by about 5 K. There is also a disparity in the magnitude of the

ΔT_{PEN} across the cell. The increased performance has increased this value by about 25 K. The general shape of the two distributions remains similar. Also expected is the increased current density of the high performance cell. As the cell becomes more active (i.e. producing more current), more heat is generated which lends evidence as to why the ΔT_{PEN} has increased in the high performance (HP) case. The PEN temperature near the fuel exit is interesting in that the HP PEN temperature has decreased below that of the LP PEN. This is due to the increased air flow rate in the HP case such that an air utilization of 0.25 is maintained. This increased flow contributes to the increased cooling at the fuel exit/air inlet.

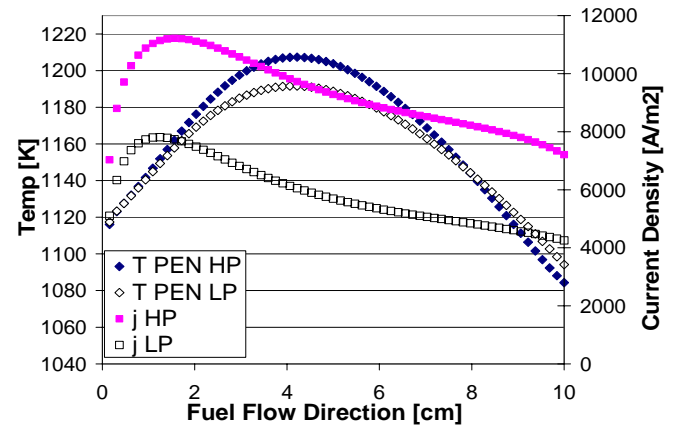


Figure 4. No pre-reforming, PEN temperature and current density distributions.

Figure 5 shows the species concentrations distributions for the HP and LP cells. In both cells, the SMR consumes methane and water in the first 2 cm of the cell while producing CO and H₂. The methane is almost fully consumed in the first 2 cm. Within this first 2 cm the WGS reaction consumes water and the CO produced by the SMR reaction to then produce CO₂ and more H₂. In the remaining 8 cm of the cell, the electrochemical reaction begins to dominate the H₂ and H₂O concentration distributions; water is produced while the H₂ is consumed. Additionally, the WGS dominates the CO and CO₂ concentration distributions in the last 8 cm by shifting CO to CO₂. In comparing the HP and LP distributions, several interesting are noteworthy. As expected the HP cell reacts more H₂ to produce higher concentrations of H₂O and lower concentrations of H₂ than seen in the LP cell. This is due directly to the electrochemical reactions. Further comparison reveals that the methane concentrations in the LP cell are lower than in the HP cell. The CO concentrations are lower in the HP cell. These results are due to the difference in the rates of electrochemical reaction between the two cells because the rate of the SMR reaction in both cells will be similar. This is evidenced by the similar average temperatures of the two cells as well as the similar temperatures seen in the first 2 cm of the cell. Hypothetically if the hydrogen is consumed at a faster rate while methane and

water are being consumed at the same rate their concentrations would rise simply because hydrogen is being consumed faster.

Figure 10 shows the various polarization distributions. The lower performance (LP) cell has a larger peak Nernst potential, which is due in part to the lower peak temperature of the LP cell. The activation losses of the HP cell are much lower than those of the LP cell as expected. The ohmic losses are greater in the HP cell than in the LP cell despite the improvements to the HP cell's resistance and the higher temperatures of the HP cell. This is due to the fact that as the current increases the voltage drop associated with the ohmic losses increases according to Ohm's law. Since the limiting current density was assumed to be equivalent in both cases, the concentration losses are higher in the HP cell because it is operating closer to the limiting current density since in the HP case there is higher current generation.

Partial Pre-Reformation

The figure below shows the HP and LP cells operating with partially pre-reformed methane. The PEN temperature distributions seen here contrast with those in the no-pre-reformation case because there is much less endothermic cooling available since there is a lower concentration of methane at the fuel inlet. The dominant cooling mechanism in this case is the convective cooling by the cathode air. The differences between the HP and LP cells are similar to the differences seen in the no pre-reformation case. The HP cell has a higher peak temperature as well as a higher current density distribution. The PEN temperature distributions are similar in shape with the PEN temperature near the fuel exit being lower in the HP case due to the increased air flow rate. The ΔT_{PEN} in the HP cell is larger than that in the LP cell by about 30 K.

The species concentration distributions are shown in Figure 7. As stated in the previous section, the methane and water are consumed by the reformation reactions resulting in decreased concentrations in the first 2 cm of the cell while hydrogen, CO, and CO₂ are being produced during this same distance. Further along the cell, the water's concentration rises as the hydrogen is electrochemically consumed. Also as before the hydrogen concentration distribution is lower in the HP case as expected.

Also similar to before is the higher concentration of methane in the HP cell, however, it is less noticeable in this case where the initial methane concentrations were not as high. Contrasting this fuel composition to the one previously mentioned, this fuel composition results in similar exit concentrations but differs near the inlet of the cell as expected.

Figure 11 shows the Nernst potential and polarization distributions along the cells. The Nernst potential is higher in the LP cell case at the fuel inlet, but as the cell cools due to the cathode air, the Nernst potential increases in the HP cell surpassing that of the LP cell. The PEN temperature largely influences this switch. This also occurred in the no pre-reformation case but to a lesser extent. The other polarization

distributions compare in a way similar to the case of no pre-reformation.

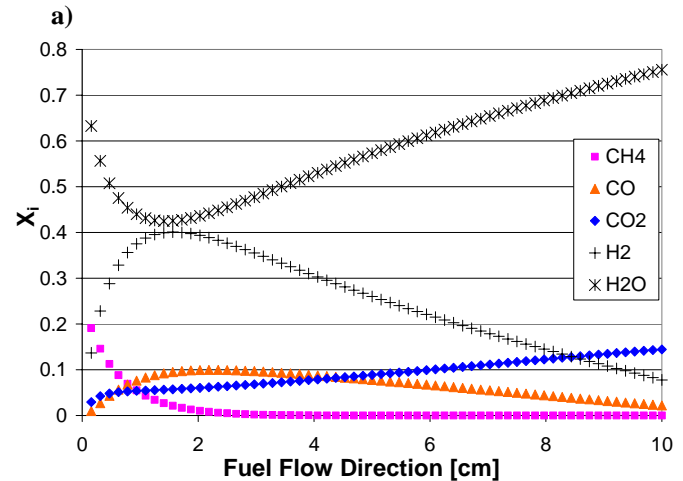
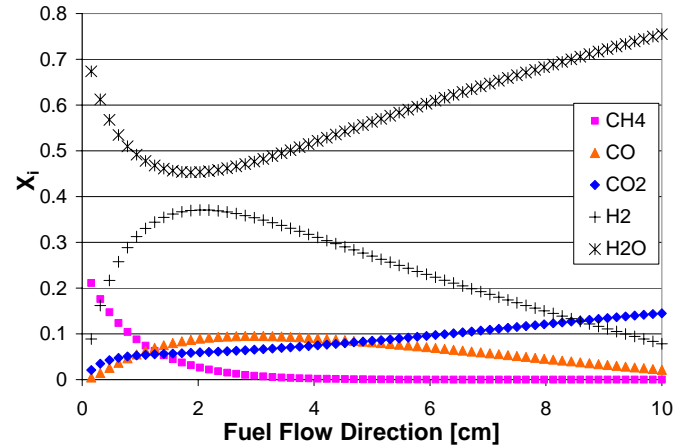


Figure 5. No pre-reforming, concentration distributions a) high and b) low performance.

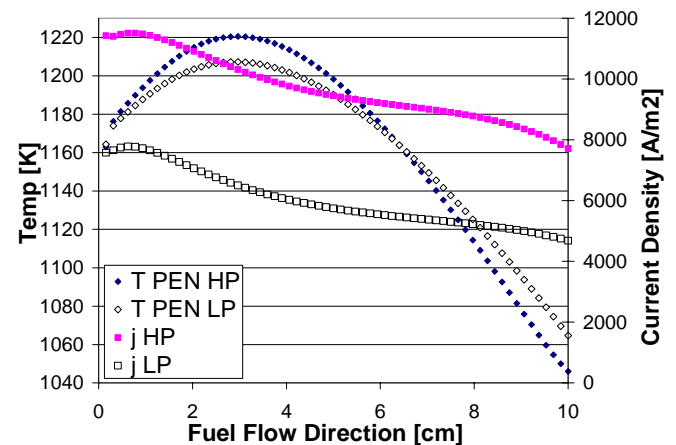


Figure 6. Partial Pre-Reformation, PEN temperature and current density distributions.

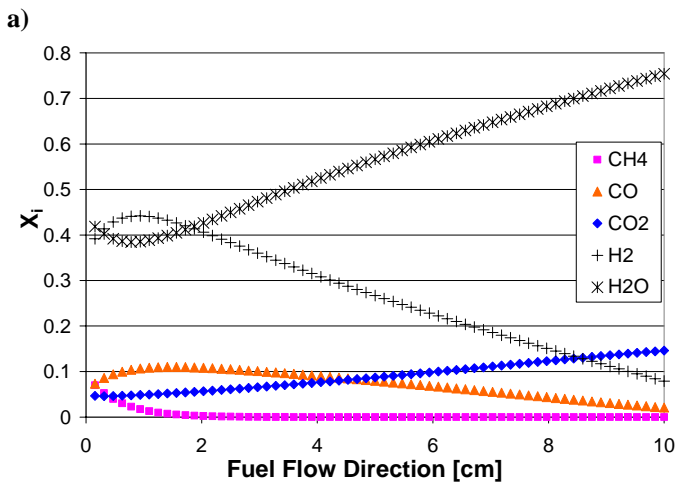
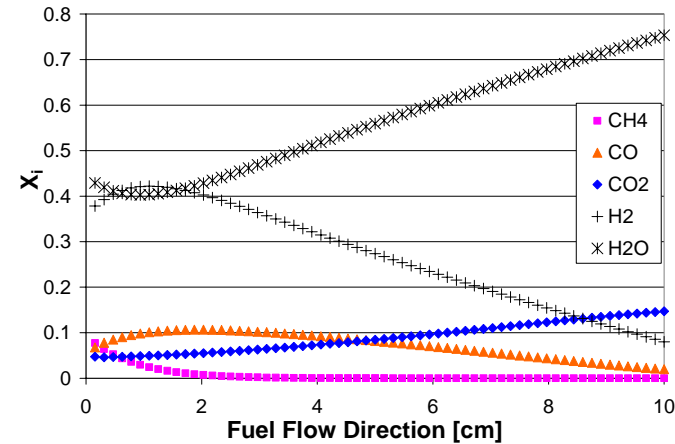


Figure 7. Partial pre-reforming, concentration distributions a) high and b) low performance.

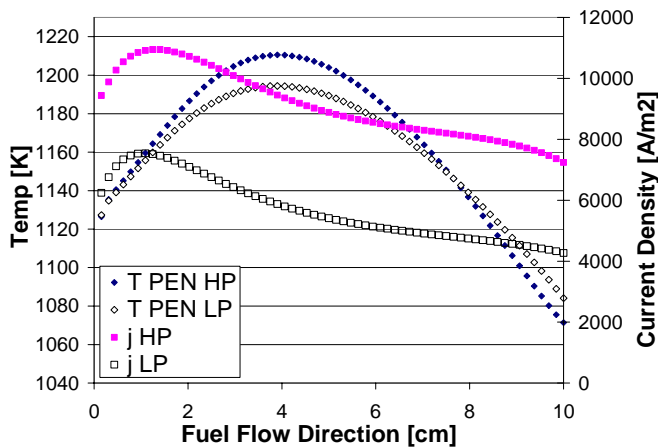


Figure 8. Syngas, PEN temperature and current density distributions.

Syngas

Figures 8, 9, and 12 show the results when using the syngas fuel composition. Again the same contrasts can be drawn between the HP and LP cells: higher max PEN temperature in the HP cell, larger ΔT_{PEN} in the HP cell (by about 29 K), lower PEN temperature near the fuel exit in the HP case, and higher current density distribution in the HP cell.

In Figures 9 and 12, the species concentration and polarization distributions are displayed. When comparing the HP and LP cells similar trends can be extracted from these figures as in the previous sections and will not be mentioned here to avoid repetition. However, some general conclusions can be surmised as to how the fuel composition affects these different distributions.

Table 7 summarizes some of the results from the various fuel compositions to allow for easier comparison. When there is more hydrogen present in the fuel, the flatter the current density and activation polarization distributions are near the fuel inlet, which would be expected. The convective cooling from the cathode gas becomes more dominant as evidenced by the more pronounced decrease in temperature at the fuel exit/air inlet. The average PEN temperatures for all the various fuel variations are similar. The maximum PEN temperature occurs closer to the fuel inlet for a higher hydrogen content. The higher the hydrogen content the more severe the ΔT_{PEN} and the maximum PEN temperature become. In the partial pre-reforming case this is probably due mostly to the increase in electrochemical activity (i.e. higher current) compared to the no pre-reforming case. However, this cannot explain the same trend in the syngas case where a lower current than the no pre-reforming case is seen while a larger max PEN temperature and ΔT_{PEN} are seen in the syngas case compared to the no pre-reforming case. This suggests something else is at play. Looking at the max T_{PEN} for the no pre-reforming case and the syngas case again, one should see that they are very similar, however the min ΔT_{PEN} for both these cases differ by a larger margin. This difference of the min T_{PEN} is due to the increased cooling capability in the syngas case caused by the nitrogen dilution of the fuel, which pulled down the min T_{PEN} . These trends show that the fuel composition can also affect the PEN temperature distribution. However, these PEN temperature distributions can be managed through control schemes such as varying the air flow rate such that a constant cathode exhaust temperature is maintained. One could also vary other parameters such as fuel utilization or fuel composition given that these parameters were not fixed and the designer only cared about the PEN temperature distribution.

The validity of this model is affirmed when comparing to other results in the literature. The concentration distributions agree with the results in literature as well as with one's intuition. However, the PEN temperature distributions in the literature are generally thought to be more extreme than what is depicted here. Comparisons to [11] show a slight disagreement near the fuel inlet for their corresponding

counter-flow model. Their results show a slight dip (or plateau) in the PEN temperature near the fuel inlet, which then gives way to a distribution similar to the one shown here but with a sharper peak. However, they use a different fuel composition and different electrochemical model among other things, but the most important difference is the difference in their cell dimensions and interconnect thickness. The cell they modeled was 40 cm long, four times the length of the cell shown here. With a longer cell, a larger maximum PEN temperature difference would be expected. The interconnect thickness as shown in the next section of this paper will also affect this. Furthermore, a rough comparison to the modeling work done by [8] shows that the trends seen here agree with the results given in that publication. The results of [8] coincide with the PEN temperature trend seen near the fuel inlet with no slight dip or plateau rather a sharp increase in PEN temperature. The cell dimensions used in [8] were the same as those used here. The fuel composition is different from that used here, and other details such as the interconnect thickness are not known. It is difficult to make any direct comparison with the models in literature, but the results shown here show similar trends to other publications.

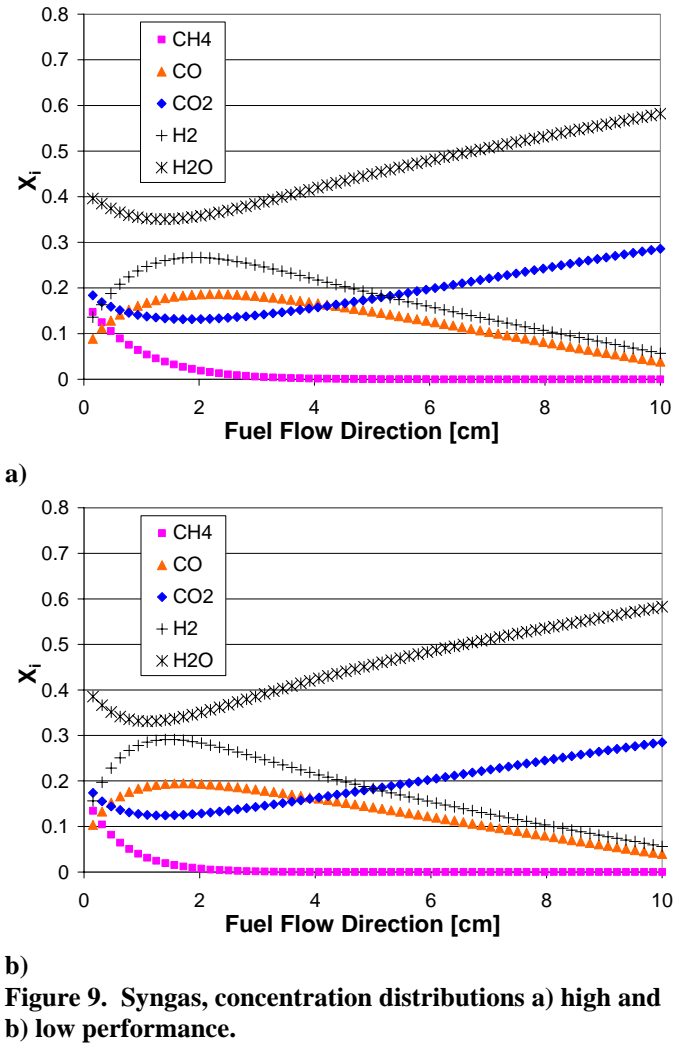


TABLE 7. FUEL COMPOSITION VARIATION SUMMARY

	HP			LP		
	NoPreRe f	PartPreRe f	Syngas	NoPreRe f	PartPreRe f	Syngas
U_f	85	85	85	85	85	85
U_a	25	25	25	25	25	25
V_{cell}	0.7	0.7	0.7	0.7	0.7	0.7
I_{cell}	2.32	2.42	2.28	1.47	1.50	1.42
$T_{PEN} \text{ avg}$	1165	1166	1165	1159	1165	1160
$T_{PEN} \text{ max}$	1207	1221	1211	1192	1207	1194
$T_{PEN} \text{ min}$	1084	1046	1071	1094	1065	1084
ΔT_{PEN}	123	174	139	97	143	110

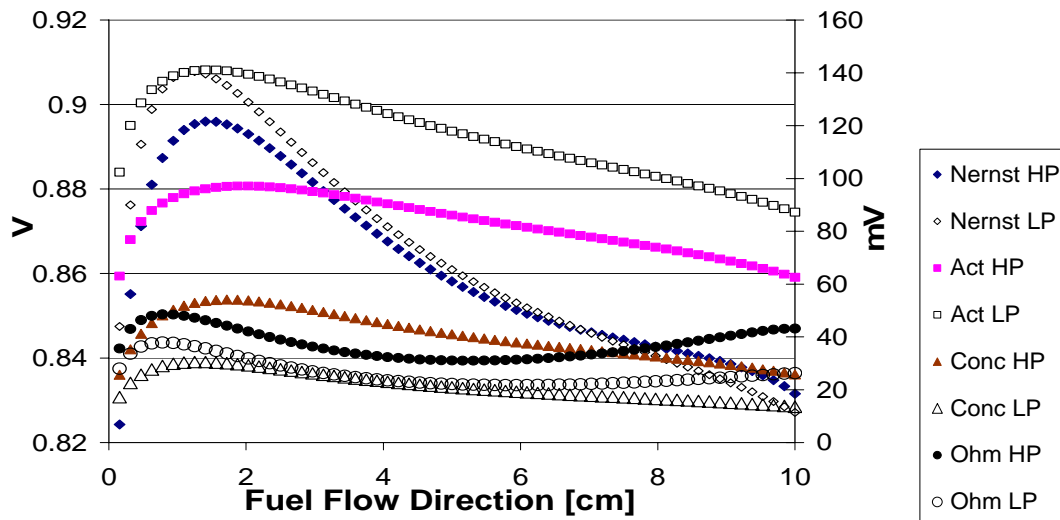


Figure 10. No pre-reforming, Nernst Potential and polarization distributions.

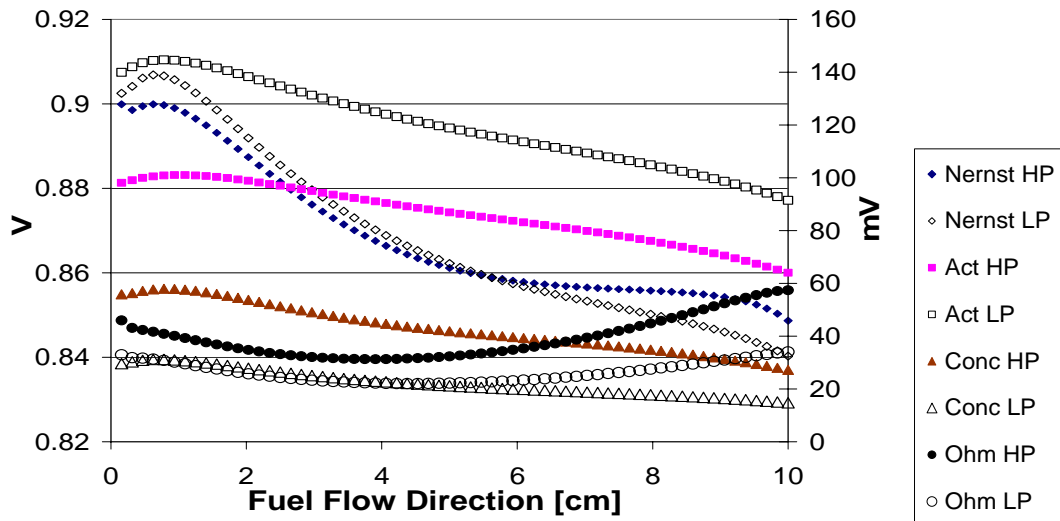


Figure 11. Partial Pre-Reformation, Nernst potential and polarization distributions.

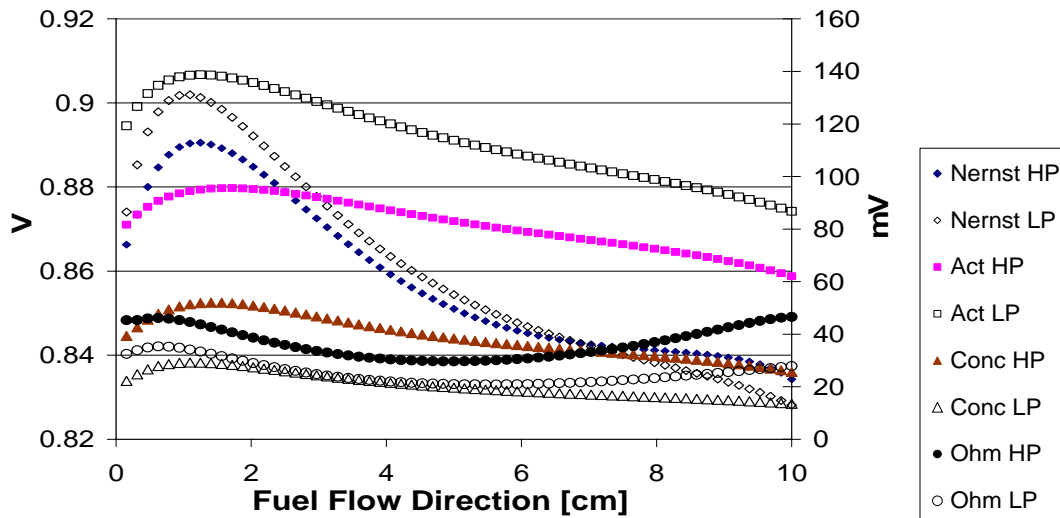


Figure 12. Syngas, Nernst potential and polarization distributions.

Physical/Dimensional Parameter Variation

In this section, the interconnect thickness and thermal conductivity are adjusted to explore the effect on the cell temperature differential. The fuel composition and the corresponding inlet temperatures were specified by the no pre-reforming case. The HP cell parameters were also used for these variations. Figures 13 and 14 show the results. The interconnect and thermal conductivity both have a marked effect on the cell temperature differential. This is expected considering that as the IC thickness or thermal conductivity is increased the resistance to heat transfer is decreased thereby allowing heat generated in a hot part of the cell to be transferred to a cool part of the cell more easily alleviating large temperature gradients throughout the cell as evidenced by the decrease in the total cross cell temperature difference. These results suggest that DIR-SOFCs should be constructed using metallic interconnects that have a considerable thickness such that severe thermal gradients are avoided. Using a ceramic interconnect would create large thermal gradients due to the low thermal conductivities of ceramics. Increases in thermal conductivity and IC thickness begin to lose their

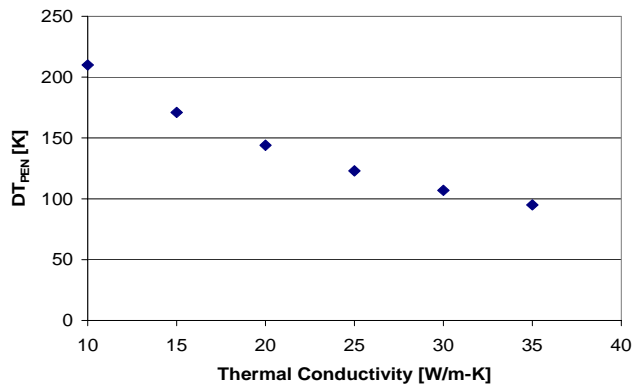


Figure 13. Thermal Conductivity Sensitivity.

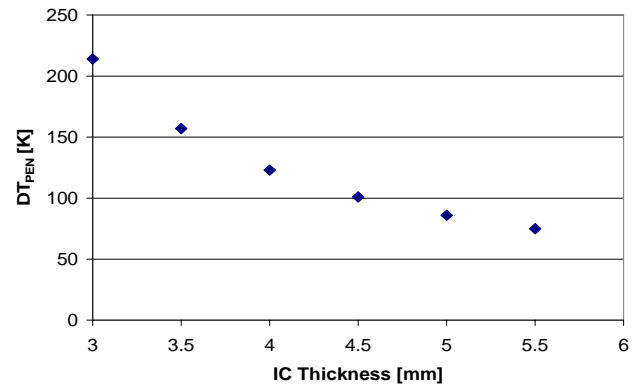


Figure 14. IC Thickness Sensitivity.

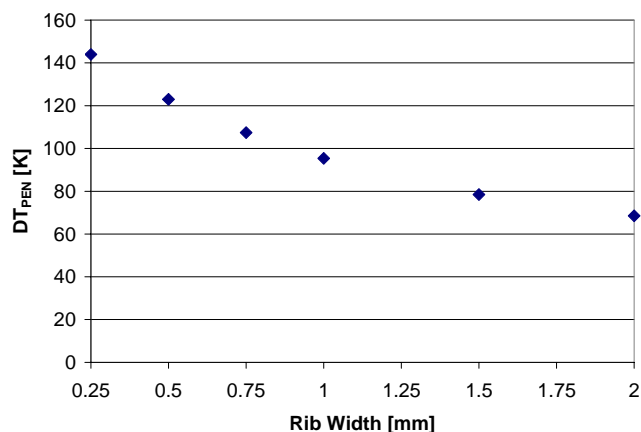


Figure 15. Rib Width Sensitivity.

Heat Loss Sensitivity

The inclusion of heat loss has been analyzed in order to assess the sensitivity of model results to this assumption. The heat loss model assumes that the heat loss occurs only at the edges of the cell where fuel and air enter and exit. The fuel used in this analysis was the no pre-reformation case, and the performance used was the HP case. The ambient temperature was varied at 850 and 950 K in order to determine the sensitivity of the model to this parameter.

Comparing Figure 16 to the corresponding figures where an adiabatic assumption is used, the peak temperature in the case of no heat loss is higher. The peak current density in the case of no heat loss is also higher but only by a slight margin. The overall current density distribution is slightly flatter in the

heat loss case with slightly higher current densities near the fuel exit. The PEN temperature distribution shows a steep drop at the fuel inlet and air inlet (fuel exit). At the fuel inlet the result is a large thermal gradient of 124 K/cm, which is larger than the gradient seen at the fuel exit. This is due to the additional cooling there resulting from the heat loss. Despite this steep drop, the total cross cell temperature difference remains close to that of the corresponding no heat loss case. However, this steep drop can still pose a threat to the longevity of the cell due to the subsequent large thermal stresses that may lead to cracking, delamination, etc.

The activation polarizations have decreased by a very small margin in the heat loss case despite the decrease in temperature seen in the heat loss case. This can be attributed to the incapability of our electrochemical model to take into account the effect of temperature on the exchange current density since we assume a constant exchange current. The ohmic polarization does increase in the heat loss case due to the reduced temperature. The concentration polarization distribution changes almost imperceptibly. The Nernst potential distribution has changed from the no heat loss case in that it has been shifted up by about 1 mV.

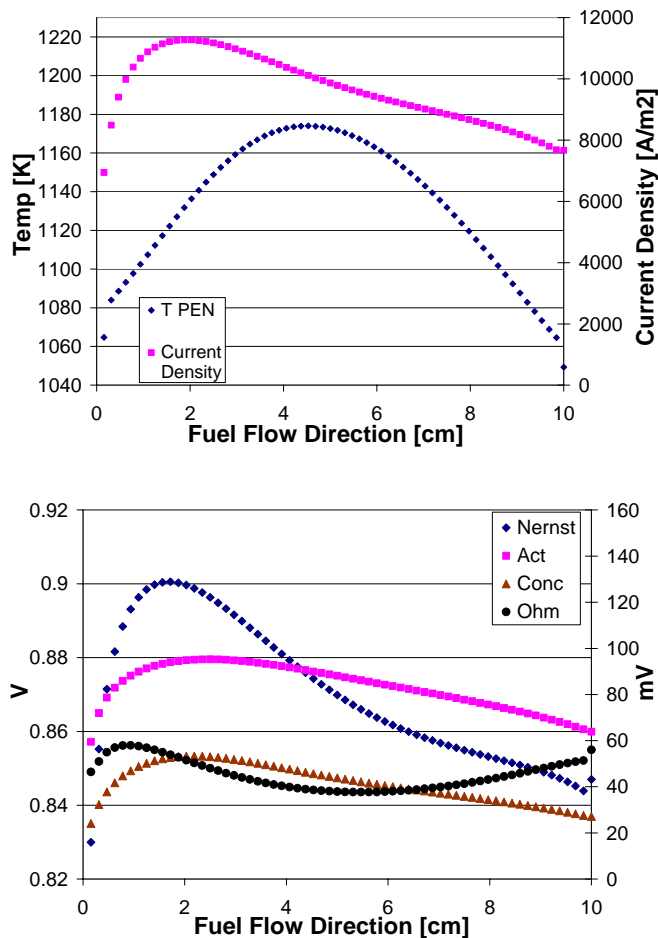


Figure 16. Heat loss with ambient temperature of 950 K.

In Figure 17, As the ambient temperature is decreased further to 850 K, the peak current density decreases below that of the case of heat loss with 950 K ambient temperature. The steep drop in the PEN temperature distribution at the fuel inlet and exit simply worsens as the ambient temperature drops (see Figure above). For an ambient temperature drop of 100 K, the large thermal gradient at the fuel inlet increases to 157 K/cm. The Nernst potentials and polarizations follow the same trends observed in the previous comparison of the heat loss and adiabatic cases. Whatever was decreased by the inclusion of heat loss was also decreased further by the decreased ambient temperature, and vice versa.

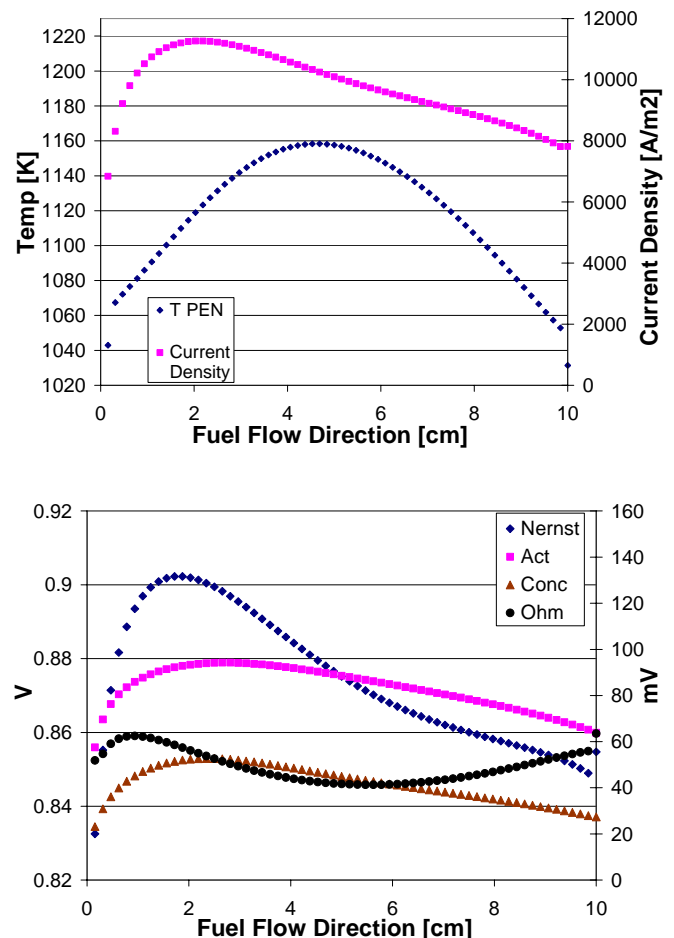


Figure 17. Heat loss with ambient temperature of 850 K.

CONCLUSIONS

A quasi-2-dimensional model has been developed to study on-anode reforming of methane in a planar SOFC. Continued improvements in the performance of SOFCs will have an effect on the temperature gradients within the PEN. In fact when the performance of the cell was improved as shown in this paper, the resulting increase in the PEN temperature differential was about 30 K for all the different fuel

compositions considered. Certain assumptions may have had an impact on these results. In particular the assumption of constant limiting current density in both the HP and LP cells may have caused some error in the results, yet confidence in a considerable increase in cell temperature differential due to increased performance is strong. The cell temperature differentials will become even worse as manufacturers make the cells larger. The cell considered in this paper was only 10 cm long and the SECA industry teams are looking at 30 by 30 cm cells. The temperature gradients within these cells could be severe. But it may be possible to mitigate these gradients by implementing effective controls and safeguards, but by also designing the stack with specific design parameters such that the ΔT_{PEN} can be minimized. This could involve effective combinations of rib width, interconnect thickness, and material properties. The adiabatic assumption commonly used in fuel cell modeling may lead to underestimation of thermal gradients especially near the inlets and exits when there is significant heat loss there. It is important to remain aware of this result when using the adiabatic assumption.

ACKNOWLEDGMENTS

We graciously acknowledge the financial support of the U.S. Department of Defense Fuel Cell Program of the Engineer Research and Development Center of the U.S. Army Corps of Engineers and our program manager, Mr. Franklin H. Holcomb.

NOMENCLATURE

A	Surface area: m^2
C	Specific heat: $kJ/(kg \cdot K)$
D_c	Characteristic diameter: m
E_0	Ideal voltage: V
E_a	Activation energy: $kJ/kmol$
\dot{E}	Energy rate: kW
F	Faraday's constant: $96,485 \text{ kC/kmol}$
Δg	Change in Gibbs free energy of reaction: $kJ/kmol$
\dot{H}	Enthalpy rate: kW
H	Convection coefficient: $kW/(m^2 \cdot K)$ or Specific enthalpy: $kJ/kmol$
i	Electrical current: kA
i_0	Exchange current density: kA/m^2
i_L	Limiting current density: kA/m^2
j	Current Density: kA/m^2
L	Length: m
K	Thermal conductivity: $kW/(m \cdot K)$
k_0	Pre-exponential constant: $kmol/(m^2 \cdot s \cdot bar)$
K_{eq}	Equilibrium constant
M	Molar mass: $kg/kmol$
N	Mole number: $kmol$
\dot{N}	Molar flow rate: $kmol/s$
Nu	Nusselt number: $(-)$
N	Electron coefficient ratio: $(-)$
P	Pressure: kPa , bar

Q	Reaction quotient
\dot{Q}	Heat transfer rate: kW
R	Reaction rate: $kmol/s$ or Resistance: Ω
R_u	Universal gas constant: $8.314 \text{ kJ/(kg} \cdot K)$
T	Temperature: K
ΔT	Change in temperature: K
t	Time: s
U	Internal energy: kJ
u	Specific internal energy: kJ/kg
V	Voltage: V or Volume: m^3
\dot{W}_{elec}	Electrical power: kW
X	Species mole fraction: $(-)$
η	Efficiency: $(-)$
H	Polarization: V
P	Density: kg/m^3
N	Stoichiometric coefficient: $(-)$

ACRONYMS

LHV	Lower Heating Value
SC	Steam-to-Carbon
PEN	Positive Electrode-Electrolyte-Negative Electrode
SOFC	Solid Oxide Fuel Cell
HP	High Performance
LP	Low Performance

REFERENCES

- [1] W.A. Surdoval, The U. S. Department of Energy fossil energy fuel cell program solid state energy conversion alliance goals and challenges, 8th Annual SECA Workshop, San Antonio, Texas, 2007.
- [2] Sangtongkitcharoen W., Assabumrungrat, S., Pavarajarn V., Laosiripojana, N., and Praserttham, P. "Comparison of carbon formation boundary in different modes of solid oxide fuel cells fueled by methane." Journal of Power Sources. Elsevier. 142 (2005) 75-80.
- [3] Laosiripojana, N. and Assabumrungrat, S. "Catalytic steam reforming of methane, methanol, and ethanol over Ni/YSZ: The possible use of these fuels in internal reforming SOFC." Journal of Power Sources. Elsevier. 163 (2007) 943-951.
- [4] Ferguson, J.R., J. M. Fiard, R. Herbin, Three-dimensional numerical simulation for various geometries of solid oxide fuel cells, Journal of Power Sources, Volume 58, Issue 2, February 1996, Pages 109-122
- [5] Mueller, F., Brouwer, J., Jabbari, F., and Samuelsen, S. "Dynamic Simulation of an Integrated Solid Oxide Fuel Cell System Including Current-Based Fuel Flow Control." Journal of Fuel Cell Science and Technology. 3 (2006) 144-154.
- [6] Daun, K.J., S.B. Beale, F. Liu, G.J. Smallwood, Radiation heat transfer in planar SOFC electrolytes, Journal of

- Power Sources, Volume 157, Issue 1, 19 June 2006, Pages 302-310.
- [7] Tanaka T., Y. Inui, A. Urata, T. Kanno, Three dimensional analysis of planar solid oxide fuel cell stack considering radiation, *Energy Conversion and Management*, Volume 48, Issue 5, May 2007.
- [8] Achenbach, E. (1994). "Three-dimensional and time-dependent simulation of a planar solid oxide fuel cell stack." *Journal of power sources* 49(1): 333.
- [9] Kim, J.W., Virkar, A.V., Fung, K.Z., Mehta, K., and Singhal, S.C. "Polarization Effects in Intermediate Anode Supported Solid Oxide Fuel Cells." *Journal of the Electrochemical Society*. 146 (1) 69-78 (1999)
- [10] Xu, J. and Froment, G. "Methane Steam Reforming, Methanation, and Water Gas Shift: I. Intrinsic Kinetics." *AIChE Journal*. 35 (1989) 88-96.
- [11] Aguiar, P., Adjiman, C. S., and Brandon, N. P. "Anode-supported intermediate temperature direct internal reforming solid oxide fuel cell. I: model-based steady-state performance." *Journal of Power Sources*. Elsevier. 138 (2004) 120-136.
- [12] Achenbach, E. and Riensche E. "Methane/steam reforming kinetics for solid oxide fuel cells." *Journal of Power Sources*. Elsevier. 52 (1994) 283-288.
- [13] Ahmed, K., Foger, K., Kinetics of internal steam reforming of methane on Ni/YSZ-based anodes for solid oxide fuel cells, *Catalysis Today*, Volume 63, Issues 2-4, 25 December 2000, Pages 479-487.
- [14] Iora, P., P. Aguiar, C.S. Adjiman, N.P. Brandon, Comparison of two IT DIR-SOFC models: Impact of variable thermodynamic, physical, and flow properties. Steady-state and dynamic analysis, *Chemical Engineering Science*, Volume 60, Issue 11, June 2005, Pages 2963-2975,
- [15] Incropera, F. and DeWitt, D. Fundamentals of Heat and Mass Transfer. 5th ed. John Wiley & Sons, Inc.: Hoboken, NJ (2002).
- [16] Ghezel-Ayagh, H. Solid Oxide Fuel Cell Program at FCE, Inc. 9th Annual SECA Workshop, Pittsburgh, Pa, 2008.
- [17] Leone, P., M. Santarelli, P. Asinari, M. Cali, R. Borchiellini, Experimental investigations of the microscopic features and polarization limiting factors of planar SOFCs with LSM and LSCF cathodes, *Journal of Power Sources*, Volume 177, Issue 1, 15 February 2008, Pages 111-122.
- [18] Laurencin, J., F. Lefebvre-Joud, G. Delette, Impact of cell design and operating conditions on the performances of SOFC fuelled with methane, *Journal of Power Sources*, Volume 177, Issue 2, 1 March 2008, Pages 355-368.